Protein Science (2000), *9*:886–897. Cambridge University Press. Printed in the USA.

Conformational flexibility in the apolipoprotein E amino-terminal domain structure determined from three new crystal forms: Implications for lipid binding

BRENT W. SEGELKE,[1] MICHAEL FORSTNER,[1,6] MARK KNAPP,[1] SERGEI D. TRAKHANOV,[1,2,3,7] SEAN PARKIN,[1,8] YVONNE M. NEWHOUSE,[2] HENRY D. BELLAMY,[4] KARL H. WEISGRABER,[2,3,5] AND BERNHARD RUPP[1]

[1]Lawrence Livermore National Laboratory, Biology and Biotechnology Research Program, L-448, University of California, Livermore, California 94550
[2]Gladstone Institute of Cardiovascular Disease, P.O. Box 419100, San Francisco, California 94141-9100
[3]Cardiovascular Research Institute, University of California, San Francisco, California 94141
[4]Stanford Synchrotron Radiation Laboratory, MS 69, P.O. Box 4349, Stanford, California 94309
[5]Department of Pathology, University of California, San Francisco, California 94141

(RECEIVED December 15, 1999; FINAL REVISION February 17, 2000; ACCEPTED March 7, 2000)

Abstract

An amino-terminal fragment of human apolipoprotein E3 (residues 1–165) has been expressed and crystallized in three different crystal forms under similar crystallization conditions. One crystal form has nearly identical cell dimensions to the previously reported orthorhombic ($P2_12_12_1$) crystal form of the amino-terminal 22 kDa fragment of apolipoprotein E (residues 1–191). A second orthorhombic crystal form ($P2_12_12_1$ with cell dimensions differing from the first form) and a trigonal ($P3_121$) crystal form were also characterized. The structures of the first orthorhombic and the trigonal form were determined by seleno-methionine multiwavelength anomalous dispersion, and the structure of the second orthorhombic form was determined by molecular replacement using the structure from the trigonal form as a search model. A combination of modern experimental and computational techniques provided high-quality electron-density maps, which revealed new features of the apolipoprotein E structure, including an unambiguously traced loop connecting helices 2 and 3 in the four-helix bundle and a number of multiconformation side chains. The three crystal forms contain a common intermolecular, antiparallel packing arrangement. The electrostatic complimentarity observed in this antiparallel packing resembles the interaction of apolipoprotein E with the monoclonal antibody 2E8 and the low density lipoprotein receptor. Superposition of the model structures from all three crystal forms reveals flexibility and pronounced kinks in helices near one end of the four-helix bundle. This mobility at one end of the molecule provides new insights into the structural changes in apolipoprotein E that occur with lipid association.

Keywords: apolipoprotein E; lipid binding; MAD phasing; X-ray crystallography

Apolipoprotein E (apoE) (M_r = 34,200, 299 amino acids) serves as a ligand for the low density lipoprotein (LDL) receptor family, and through this interaction, plays a major role in modulating plasma lipoprotein metabolism (Mahley, 1988; Weisgraber, 1994). ApoE is polymorphic with three major isoforms (apoE2, apoE3, and apoE4) and a number of rare variants (Mahley, 1988; Rall & Mahley, 1992; Weisgraber, 1994). The major apoE isoforms differ at positions 112 and 158, where apoE3 contains cysteine and arginine, respectively, and apoE2 contains cysteine and apoE4 arginine at both positions (Weisgraber et al., 1981). This polymorphism has functional consequences. ApoE2 binds defectively to the LDL receptor, resulting in type III hyperlipoproteinemia, a lipid disorder associated with premature heart disease (Mahley & Rall, 1995). This defective binding results from the substitution of arginine by cysteine at position 158 and is mediated indirectly, through rearrangement of salt bridges (Wilson et al., 1994; Dong et al., 1996). ApoE4 is associated with increased lipid levels and an increased risk of cardiovascular disease (Utermann et al., 1984; Eichner et al., 1993; Luc et al., 1994) and is also a major risk factor for Alzheimer's disease (Corder et al., 1993; Saunders et al., 1993; Strittmatter et al., 1993) and other forms of neurodegeneration (Mayeux et al., 1995; Slooter et al., 1997; Teasdale et al., 1997).

ApoE is composed of two functionally distinct domains (Aggerbeck et al., 1988; Wetterau et al., 1988). Thrombin cleavage of apoE results in a 22 kDa amino-terminal domain (residues 1–191)

Reprint requests to: Bernhard Rupp, Lawrence Livermore National Laboratory, Biology and Biotechnology Research Program, L-452, University of California, Livermore, California 94550; e-mail: br@llnl.gov.
[6]Present address: Department of Molecular Biology, Biomedical Center, Box 590, S-75124 Uppsala, Sweden.
[7]Present address: RIKEN Harima Institute, Hyogo 679-5143, Japan.
[8]Present address: Department of Chemistry, University of Kentucky, Lexington, Kentucky 40506.

and a shorter 10 kDa carboxy-terminal fragment (residues 216–299) (Innerarity et al., 1983). The 22 kDa domain contains the LDL receptor–binding region (vicinity of residues 136–150) (Mahley, 1988; Weisgraber, 1994). The 10 kDa fragment carries the major lipid-binding determinants of apoE (Weisgraber, 1990) and is responsible for the tetramerization of the intact apoE protein (Aggerbeck et al., 1988). The three-dimensional (3D) structure of the 10-kDa fragment is not known, although it has recently been crystallized (Forstner et al., 1999). Predictions of the secondary structure of this domain (Rall et al., 1982; Segrest et al., 1992) agree with circular dichroism (CD) data indicating it is mostly α-helical (Aggerbeck et al., 1988).

The crystal structure of the 22 kDa amino-terminal domain of apoE has been determined (Wilson et al., 1991). The protein forms an elongated, antiparallel four-helix bundle with a short connecting helix between helices H1 and H2. Based on this initial model, we recently refined the structures of the 22 kD fragment of apoE3 and an apoE2 D154A mutant (Dong et al., 1996). However, neither Wilson et al. (1991) nor we were able to unambiguously trace amino-terminal residues 1–22, the connecting loop between helices H2 and H3 (residues 82–91), or the terminal 25 residues (166–191). The missing portions are located in the same region of the molecule, with weak or undefined electron density at one extreme of the helix bundle, and amount to nearly 30% of the 22 kDa fragment.

Like other soluble apolipoproteins, apoE is stable in both lipid-associated and lipid-free aqueous states. The helices in the four-helix bundle of apoE are amphipathic, classified as G* by Segrest et al. (1994), placing them between the typical globular amphipathic helices and the helices typical of other apolipoproteins. The amphipathic nature and particular character of the apolipoprotein helices are thought to be responsible for their lipid-binding properties (Segrest et al., 1994).

It has been hypothesized that the amino-terminal four-helix bundle undergoes a significant conformational change, opening to expose the hydrophobic core to interact with lipid (Weisgraber, 1994). Molecular area measurements at an air:water interface support this model (Weisgraber, 1994). The postulated conformational change is similar to that proposed for apolipophorin III (apoLpIII), an insect apolipoprotein that exists as a five-helix bundle in the lipid-free state (Breiter et al., 1991; Wang et al., 1997). Although the major lipid-binding elements of apoE are contained in the carboxyl-terminal domain, the 22 kDa domain, the 10 kDa fragment, and the intact protein will remodel spherical vesicles of dimyristoylphosphatidylcholine (DMPC) and other phospholipids into bilayer discoidal particles (Innerarity et al., 1979, 1983). The conformation of apoE on these phospholipid discs, while of great interest, is unknown. Two models have been proposed: the "picket fence" model, in which the amphipathic helices are aligned parallel to the phospholipid acyl chains (De Pauw et al., 1995), and the "belt" model, in which the helices lie perpendicular to the acyl chains (Raussens et al., 1998).

In addition to its roles in cardiovascular and neurodegenerative diseases, apoE has been implicated in immunoregulation (Hui et al., 1980; Avila et al., 1982), modulation of intracellular cholesterol metabolism (Reyland & Williams, 1991), and control of cell growth and migration (Ishigami et al., 1998). These diverse roles underscore the importance of apoE as a potential target for therapeutic agents and highlight the need for a better understanding of the relationship of its structure and function. In this study, in an effort to obtain a more detailed structure of the amino-terminal domain, which contains the LDL receptor–binding region, we sought to engineer a truncation mutant (1–165) to eliminate potential complications arising from the ill-defined carboxyl-terminal region of the 22 kDa fragment; to screen for different crystal forms; and to re-determine the structure from all crystal forms, taking full advantage of the newest experimental and computational techniques. We pursued multiple crystal forms because apoE is thought to undergo significant conformational changes upon binding to lipid (Weisgraber, 1994). By determining structures from multiple crystal forms, the potential existed to characterize mobility within the molecule in the lipid-free state. Three different crystal forms of the amino-terminal 165 truncation were obtained, and their structures were determined. The newly determined structures provide greater detail and higher resolution than the original 22 kDa amino-terminal structure (Wilson et al., 1991). The collection of structures from all crystal forms also provides new insight into a structural flexibility in the molecule. Comparisons of the three newly determined structures reveal common intermolecular packing interactions and kinks or hinges within the helical bundle, distinguishing two regions of the molecule.

Results

The structure of the apoE 165 fragment (Fig. 1) was determined by seleno-methiomine (Se-Met) multiwavelength anomalous disper-

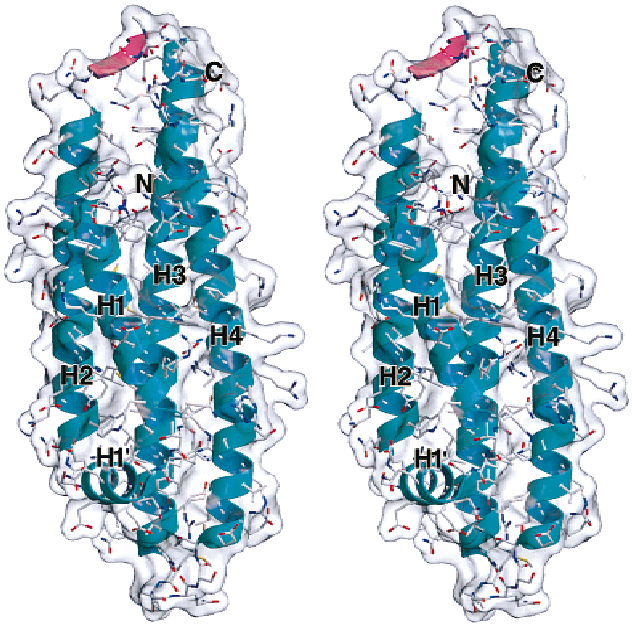

Fig. 1. ApoE3 four-helix bundle. Parallel stereo ribbon diagram, overlaid with molecular surface, of the antiparallel four-helix bundle of apoE3 in the ortho-1 crystal form. Helical segments (cyan) are labeled H1, H2, H3, and H4, with a short helix H1′ connecting H1 and H2. The single β-strand (magenta) covering most of the 80s loop (connecting helices H2 and H3) is represented as a strand because the local backbone conformations fall into the β region of the Ramachandran plot (Ramachandran et al., 1963). Two intramolecular main-chain–side-chain hydrogen bonds maintain the β-like structure. The model shown covers residues 22–165 of the amino-terminal apoE3 165 fragment. Residues 1–21 are completely absent in the experimental electron density and therefore not modeled. In this view, a number of modeled multiconformation side chains are apparent near the amino-terminal end of H4. This figure was generated with MOLSCRIPT (Kraulis, 1991), SPOCK (Christopher, 1997), and RASTER3D (Merritt & Bacon, 1997).

sion (MAD) (Hendrickson & Ogata, 1997) to 1.85 and 1.7 Å resolution for the ortho-1 (Protein Data Bank (PDB) accession code 1BZ4) and trigonal (PDB accession code 1OR3) crystal forms, respectively (Table 1). The structure of the ortho-2 form was determined to 2.5 Å resolution (accession code 1OR2) by molecular replacement (MR) using the trigonal model as a probe. All three crystal forms have a single molecule per asymmetric unit.

Quality assessment

The absence of a molecular replacement solution of the trigonal form with any of the available apoE models (Wilson et al., 1991; Dong et al., 1996) was an early indication of significant structural variability necessitating *de-novo* phasing of the structures and thorough analysis of their quality. Since 1991, when the structure of the 22 kDa fragment of apoE3 was initially determined (Wilson et al., 1991), innovations in crystallography have enabled us to minimize experimental error and to provide more detailed models. Use of cryo-cooling techniques (Parkin & Hope, 1998) and Se-Met MAD phasing (Hendrickson & Ogata, 1997) has yielded superior experimental phases to high resolution for the ortho-1 and trigonal forms (Table 2; Fig. 2A). Application of R_{free} cross-validation (Brünger, 1992a), along with maximum likelihood (ML) and phase-restrained refinements (REFMAC) (Murshudov et al., 1997) help to minimize overfitting, avoiding model bias and loss of interpretable electron density.

The R value and R_{free} (monitored throughout, 10% test set) were within expected ranges for the resolution (Table 1) and were highly correlated. Lower R factors can be (and have been) achieved, but always at the expense of R_{free} and/or correlation between R and R_{free}. X-PLOR (Brünger, 1992b) and PROCHECK (CCP4, 1994) were used to assess the agreement root-mean-square deviation (RMSD) between observed and expected bond lengths, bond angles, and the stereochemistry (Table 1). In addition, a WHATCHECK report (Vriend, 1990) for each structure was provided by the Protein Data Bank. All PROCHECK analyses were either in the expected range or better for the given resolution. All but a few modeled residues in all three crystal structures have most-favored backbone conformation, and none have disallowed conformations. Mean coordinate errors and cross-validated mean coordinate errors were estimated from Luzzati plots (Luzzati, 1953) (Table 1). The average of the individual isotropic B values is high for the ortho-2 and trigonal structures and corresponds to the mean B values calculated from the data (Blundell & Johnson, 1976), reflecting the inherent flexibility within the molecule.

Despite the improved resolution from 2.5 Å for the initial apoE3 22 kDa fragment structure (Wilson et al., 1991) to 1.73 Å for the trigonal structure, and despite improved crystallographic techniques, the amino-terminal 21 residues are not found in any of the crystal forms, indicating that the amino terminus is very likely not in a defined conformation. The H2–H3 connecting loop, or 80s loop, is also absent in the ortho-2 and trigonal forms. It is clearly traceable, however, in the ortho-1 structure from SOLOMON (Abrahams & Leslie, 1996) maps (Fig. 3). The residues of the 80s loop adopt a pseudo-β structure with side-chain–main-chain hydrogen bonds stabilizing the β-conformation. It is interesting to note the similarity between the structure for the 80s loop in our ortho-1 model and the original model of the apoE3 22 kDa fragment (Wilson et al., 1991). The initial report of the structure cautioned that the electron density for the 80s loop was poorly defined and that the coordinates "may be somewhat in error." There is in fact good

Table 1. *Native data and refinement statistics*

	Crystal form		
	Ortho-1	Ortho-2	Trigonal
Unit cell dimensions (Å)			
a	40.8	47.7	47.4
b	53.2	55.6	47.4
c	84.8	63.6	104.4
Space group	$P2_12_12_1$	$P2_12_12_1$	$P3_121$
Resolution (Å)[a]	1.85	2.50	1.73
Average B Wilson (atomic) (Å^2)[b]	18.1 (26.8)	74.6 (72.4)	40.3 (53.7)
Completeness ($F > 2\sigma$) (%)	99.1 (93.4)	93.8 (89.5)	97.2 (89.9)
No. of observations	81,518	39,148	48,854
No. of unique reflections	16,493	5,913	16,782
R_{sym} (%)[c]	3.7	6.9	6.8
Reflections/parameters[d]	2.8	1.2	2.6
R-factor (%)	20.7	25.2	22.9
R_{free}-factor (%)	24.5	29.6	23.8
RMSD bond length (Å)	0.006	0.019	0.006
RMSD bond angle (°)	1.0	2.5	1.1
Φ/Ψ most favored (%)	97.0	93.4	96.0
Mean coordinate error (Å)[e]	0.21 (0.25)	0.4 (0.44)	0.27 (0.28)

[a] Resolution given is the high-resolution cut-off for the last bin, which has $\langle I \rangle > 2\sigma$.
[b] Blundell (1976).
[c] $R_{sym} = \Sigma_i(\Sigma_j|I_{ij} - \langle I_i \rangle|)/\Sigma_i\langle I_i \rangle$.
[d] Working set only and $F > 2\sigma$.
[e] Luzzati (1953), cross-validated values in parenthesis.

Table 2. *MAD phasing statistics*

	Low	f'[a]	f''[b]	High
Ortho-1 form				
Wavelength (Å)	1.0688	0.9800	0.9796	0.9252
Resolution (Å)	2.5	2.5	2.5	2.5
No. of observations	48,125	49,494	48,828	48,674
No. of unique reflections	5,707	5,632	5,707	5,567
Completeness (%)	83.8	82.7	83.0	81.7
R_{sym} (%)	4.0	4.7	6.7	7.0
Phasing power	Reference	6.30	4.48	0.03
Phasing power anomalous	1.92	2.78	4.02	3.90
R_{Cullis}	N.A.[c]	0.31	0.45	0.76
Overall FOM[d]				
Acentric	0.7			
Centric	0.6			
Trigonal form				
Wavelength (Å)	0.9989	0.9800	0.9794	0.9566
Resolution (Å)	2.0	2.0	2.0	2.0
No. of observations	188,709	218,080	213,486	96,050
No. of unique reflections	9,835	9,806	9,806	9,798
Completeness (%)	99.8	100.0	100.0	99.6
R_{sym} (%)	7.9	8.2	8.3	7.9
Phasing power	Reference	2.85	1.31	0.27
Phasing power anomalous	0.88	2.13	2.35	2.33
R_{Cullis}	N.A.	0.55	0.81	0.95
Overall FOM				
Acentric	0.65			
Centric	0.53			

[a] f' is the wavelength at which there is a minimum in the Kramers–Kronig integration of the X-ray absorption scan of the selenium absorption edge.
[b] f'' is the wavelength at the fluorescence signal maximum in the X-ray absorption scan at the selenium absorption edge.
[c] N.A., not applicable.
[d] FOM = $|F(hkl)_{\text{best}}|/|F(hkl)|$.

agreement for the 80s loop between the previous model and our ortho-1 model.

Discussion

Packing comparison

Comparison of the packing arrangements in three crystal forms revealed significant differences: no two crystal forms can be related by simple expansion or compression of the unit cell (Fig. 4). However, all three crystal forms share a similar, antiparallel arrangement of contacting, symmetry-related helix bundles propagating through the crystal to form antiparallel sheets of stacked bundles. In both the trigonal and ortho-1 crystal forms, the principal axes of the helix form a flat sheet, whereas in the ortho-2 crystal form, they are slightly out of plane, creating a pleated sheet.

Several questions arose from the common antiparallel packing arrangement. Is the packing a specific, persistent intermolecular interaction, an electrostatic interaction, or an entropic phenomenon? Intuitively, it might appear entropically favorable for elongated objects to line up parallel or antiparallel to each other, like matchsticks when shaken in a matchbox. However, closer examination of specific contacts within these packing arrangements revealed a similar (but not identical) electrostatic interaction (Fig. 5A) among the three crystal forms, involving the carboxyl-terminal end of helix H2 and the amino-terminal end or the middle of helix H4 of a symmetry-related molecule. In the trigonal and the ortho-2 forms, the carboxyl terminal of H2 residues 76–81 are in contact distance (<5 Å) of H4 residues 143–150 of an equivalent copy. In the ortho-1 form, H2 residues 70–81 are in proximity of residues H4 136–144 of a symmetry-related molecule. Differences complicating a generalization of the packing scheme are depicted in Figure 5B. Taking one of the helix bundles from each crystal form and a symmetry-related copy of the respective contacting molecule and viewing such a packing element as a pseudodimer, we found that none of the three pseudo-dimers overlap. The pseudodimer of ortho-2 differs from that of ortho-1 by a small translational shift, while the pseudodimer of the trigonal crystal form is related to that of ortho-1 by an additional rotation of nearly 90°.

In contrast to specific differences in the details of each crystal packing, a general electrostatic interaction pattern emerges. Plotting the electrostatic isocontours at relatively low potential (Fig. 5A) reveals a longitudinal distribution of potential with a negative lobe covering helices H1, H1′, and H2 and a positive lobe covering helices H3 and H4. The distribution of potential supports the arrangement of molecules such that helices H1 and H2 interact with helices H3 and H4, as depicted for the orthorhombic forms in Figure 5C. The interactions represent the juxtapositioning of a

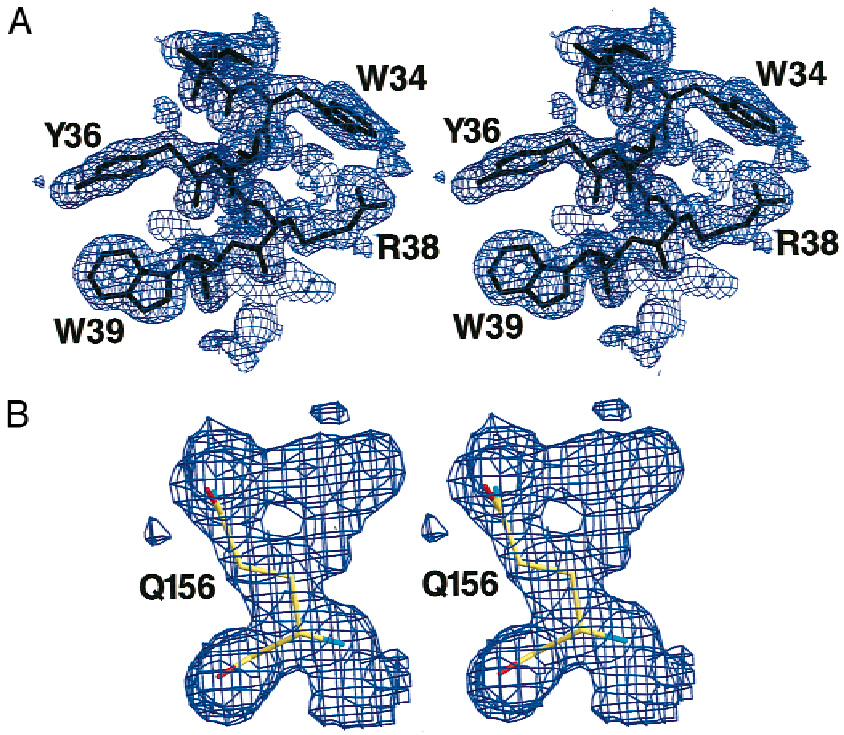

Fig. 2. Initial electron density maps and wARP. **A:** A section of the initial density modified map for the ortho-1 crystal form generated with SOLOMON (Abrahams & Leslie, 1996). The map envelops the middle portion of the H1 helix from the final ortho-1 model. The likely contributors to the exceptional quality of such experimental maps are cryo-cooling, MAD phasing, ML heavy atom refinement, and solvent flipping density modification. For both the ortho-1 and trigonal crystal forms, ML heavy atom refinement and solvent flipping density modification give better quality maps than more traditional methods. This figure was generated by XtalView (McRee, 1992) and RASTER3D (Merritt & Bacon, 1997). **B:** wARP map covering residue Q156. Shown here is the electron density of an obvious multiconformation that had not yet been modeled for Q156 of the apoE 165 fragment in the ortho-1 crystal form. To generate this map, we applied random perturbation of 0–0.5 Å in each *x*, *y*, and *z* direction (RMSD ~0.25 Å) to all coordinate positions of the current model. Ten percent of all model atoms were chosen at random and deleted. The resulting model was treated by multiple iterations of ARP (Lamzin & Wilson, 1993) and unrestrained REFMAC refinement (Murshudov et al., 1997). The entire procedure, starting with the random perturbation of coordinates, was repeated six times. The calculated structure factors from all six structures were averaged by wARP-weighted averaging (Perrakis et al., 1997) to generate a wARP phase and a weight. The maps shown are w Fo PHIc maps, where w and PHIc are determined by the wARP averaging. This figure was generated with XTALVIEW (McRee, 1992) and RASTER3D (Merritt & Bacon, 1997).

patch of negatively charged residues (E77, E79, and E80) with positively charged residues (R136, H140, K143, K146, R147, and R150). The same potential distribution can also lead to an arrangement in which the opposing lobes are staggered (Fig. 5C). A similar electrostatic complementarity was proposed for the interaction between apoE and the 2E8 FAB (Raffaï et al., 1995; Trakhanov et al., 1999) and between apoE and the LDL receptor (Mahley, 1988). The collection of basic residues 136–150, in fact, makes up the LDL receptor–binding region of the molecule (Mahley, 1988; Weisgraber, 1994).

Superposition

Comparison of the individual models by superposition reveals a fair amount of variation (1.8 Å RMSD between the ortho-1 and the trigonal forms, 1.8 Å RMSD between the ortho-2 and the ortho-1 forms, and 0.33 Å RMSD between the ortho-2 and the trigonal forms for all C_α atoms in common) (Fig. 6). In contrast, the RMSD of ortho-1 from an independently refined amino-terminal 22 kDa fragment of the same crystal form (accession code 1NFN) is only 0.22 Å on C_αs, consistent with the expected mean coordinate error for independent refinements. Although overall the structures differ significantly from each other and have several multiconformation side chains (Figs. 1, 2), individually superimposed sections (similar to a sliding frame) match quite closely. The flexible molecule displays slight supertwisting or untwisting around the principal axis of the helix bundle (Fig. 6A) and a notable kinking, of both helices H2 and H3 (Fig. 6B).

If the trigonal and ortho-1 models are compared (the ortho-2 form is essentially identical to the trigonal form for this purpose), the lower portions of the molecules (Fig. 6B) superimpose significantly better than the top section. The previously reported kink at Gly106 (Wilson et al., 1991) in helix H3 is most obvious in this comparison, and helix H2 also has a pronounced kink in the trigonal structure (Fig. 6C). In fact, the upper part of the molecule (the 80s loop proximal end) can be viewed as a structural unit separate from the lower portion. The lower portion is a nearly classic, full four-helix bundle, matching the approximate size and compactness of four-helix bundles from other globular proteins (Harris et al., 1994). This part of the molecule has relatively low observed *B* values

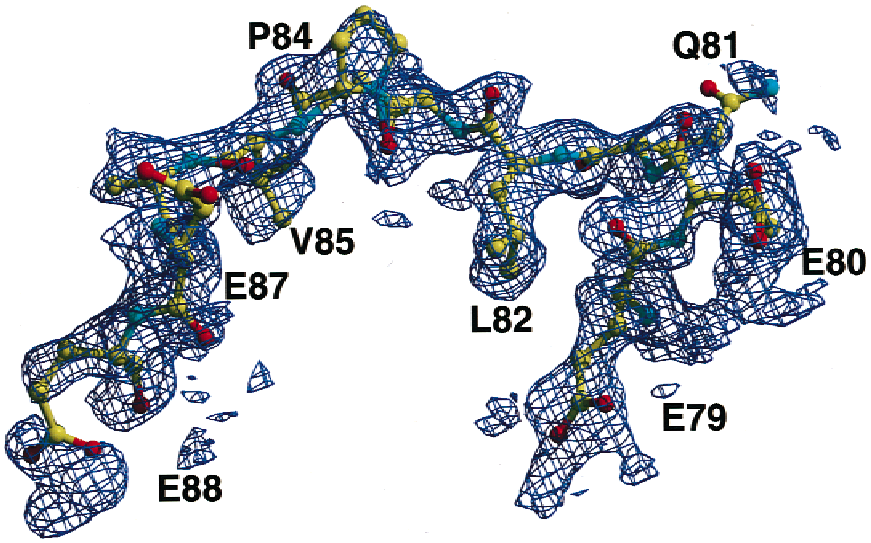

Fig. 3. SOLOMON map covering 80s loop. The initial map after density modification and phase extension with SOLOMON (Abrahams & Leslie, 1996) shows the 80s loop is clearly traceable in model-free maps. The H2–H3 connecting loop, or 80s loop, has not been previously observed in any of the numerous structure determinations of apoE and variants. The quality of this map demonstrates clearly the advantage of current crystallographic techniques for revealing new details. The 80s loop adopts a pseudo-β conformation that is stabilized by side-chain–main-chain hydrogen bonds (not shown). The 80s loop is rich in acidic residues and is probably involved in initial lipid binding through charge complementarity with positively charged phosphatidylcholine head groups.

as well. The upper portion is no longer a complete four-helix bundle, as the H1 helix terminates, leaving only three helices packed together. The *B* factors become high approaching the 80s loop in all three crystal forms as well as in the previously reported structures (Fig. 7). The 80s loop is completely defined in only one (ortho-1; Fig. 3) of the several crystal structures of apoE or its variants (Wilson et al., 1991, 1994; Dong et al., 1994, 1996).

Conformational changes upon lipid binding

The separation of the molecule into two distinct regions with different stabilities is potentially important for understanding the function of apoE. Conformational changes are thought to be critically important for both the lipid-binding and receptor-binding function of apoE. Upon binding to DMPC, the helix bundle is thought to open, allowing the hydrophobic residues (which are packed in the core of the bundle in the aqueous state) to interact with the acyl chains of the phospholipid (Weisgraber, 1994). Molecular area measurements at an air:water interface (Weisgraber et al., 1992) and disulfide bond cross-linking studies of moth apoLpIII (Narayanaswami et al., 1996), an insect apolipoprotein with similar lipid binding behavior as apoE, suggest a model involving bundle opening. The model draws additional support from the fact that, upon opening of the hydrophobic core, the molecule maintains practically the same percentage of helical character in the lipid-free state as in the lipid-bound state (determined by CD; Aggerbeck et al., 1988). The bundle has thus been suggested to open by "unzipping," leaving the secondary structure intact while exposing the hydrophobic core of the bundle to lipid. An unambiguous assignment of the "hinge region" in the molecule, however, could not be made in the case of ApoE-22k (Fig. 17 in Weisgraber, 1994, illustrates only one example of conceivable arrangements), nor is there agreement on the final conformation and arrangement of the helices on a phospholipid disc [i.e., the "belt" (Raussens et al., 1998) or "picket fence" model (De Pauw et al., 1995)].

Comparison of ApoE-22K and apoLpIII, and assignment of hinge region

High experimental *B* values from the crystal structure apoLpIII from *Locusta migratoria* (Breiter et al., 1991) also indicate greater mobility at one end of the molecule (Fig. 7B). Cross-linking the mobile end of moth apoLpIII (Fig. 7C) with an engineered disulfide link abolishes lipid binding to a lipoprotein vesicle surface. The disulfide-linked mutant can still bind to DMPC discs, indicating different modes of interaction of apoLpIII with discs or spherical lipid vesicles (Narayanaswami et al., 1996). Structural studies on insect apolipophorins (Breiter et al., 1991, Fig. 7B; Wang et al., 1997, Fig. 7C) implicate certain hydrophobic resides in initial lipid binding. In either case, the proposed open, lipid bound structure hinges at the loops distal to the flexible end (Breiter et al., 1991; Wang et al., 1997) of the molecule.

Based on the increased mobility we demonstrated for one part of apoE-22k, we propose a similar mechanism, in which the flexible end of apoE-22k initiates the opening of the helix bundle upon binding to a spherical, preformed lipoprotein particle. Assigning the flexible domain as initiation site for lipid binding and subsequent bundle opening also explains previously unresolved contradictory findings, in which a correspondence of apoE and apoLpIII was expected based on their superposition and presumed equivalence of the short nine-residue helix H1′ connecting helices H2 and H3 in apoE with the six-residue helix H3′ connecting H3 and H4 in moth apoLpIII, respectively (Narayanaswami et al., 1999). Closer inspection of such a superposition reveals that neither the direction of the chain tracing nor the crucial correspondence of the flexible regions of the molecules (Fig. 7A,B) is maintained. A

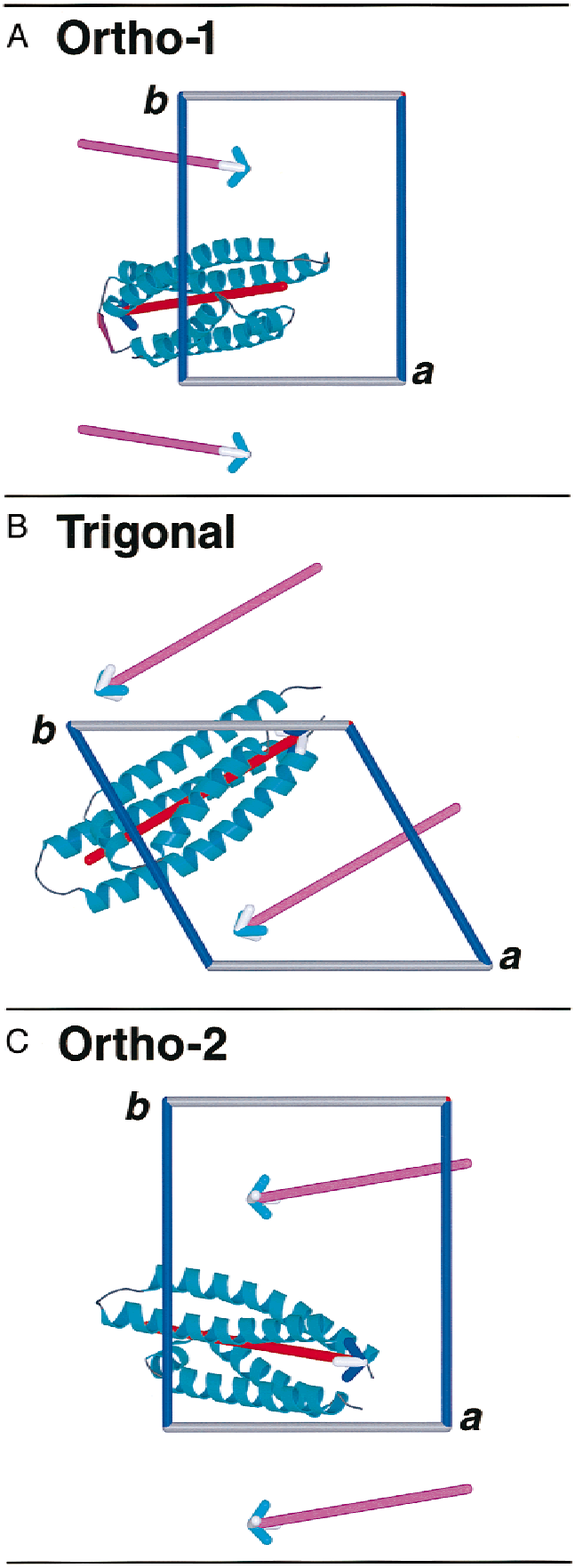

corresponding short connecting helix is also noticeably absent in the locust apoLpIII X-ray structure (Breiter et al., 1991). The two short, connecting helices in apoE and moth apoLpIII do not appear to be functionally equivalent. In moth apoLpIII, this helix is in the flexible region of the molecule and it plays a role in lipid binding. In apoE, however, the connecting helix is at the stable end of the molecule and not likely to be involved in the initial steps of lipid binding.

More speculative support for our choice of the 80s loop region in ApoE as a site for initial lipid interaction is based on possible electrostatic interactions between the flexible end of the molecules and the lipid particles. Phospholipid particles in solution do not present the hydrophobic acyl chains but the polar head groups to the solvent. The largest negative potential in apoE in fact occurs at the 80s loop, where five glutamic acid residues occur in a stretch of 12 residues in ApoE (Fig. 3). A similar grouping of negative glutamic acid residues exists in the corresponding region of locust ApoLpIII, and on the H3′ helix of moth apoLpIII. The negative charges could complement the positive charge on phosphatidylcholine head groups in lipid vesicles. Thus, it is conceivable that the negative charges and the resulting (long-range) electrostatic interaction on the flexible 80s loop in apoE initiate the binding to lipid vesicles and trigger the opening of the helix bundle, with hydrophobic (short range) interactions, playing a role in the subsequent association of the opening helices with the lipid particles.

Summary and conclusions

The structure of an amino-terminal fragment of apoE3 has been determined from three crystal forms. The structures were determined de novo for two of the crystal forms and by MR for the third form. A number of new techniques, previously not applied to structural studies of apoE, have yielded experimental maps of superior quality and high-quality model structures. Examination of packing arrangements within the three crystal forms reveal a common antiparallel packing of helix bundles along the principal axes, creating a propagating antiparallel sheet of staggered molecules. The packing is governed predominantly by nonspecific electrostatic interaction. Comparison of the three models from each of the three crystal forms reveals a large degree of conformational flexibility at one end of the molecule and kinks or hinges in helices H2 and H3. These kinks, along with the high experimental *B* values and the electronegative character of the 80s loop end of the molecule, suggest that the flexible end of the apoE molecule is the initial site for lipid binding and initiates the opening of the four-helix bundle as the conformation of apoE is reorganized on a lipid surface.

Fig. 4. Packing arrangements in three crystal forms. Projection of the crystal's unit cell for the **(A)** ortho-1, **(B)** trigonal, and **(C)** ortho-2 crystal forms. The asymmetric unit is represented both as a ribbon diagram of the four-helix bundle and as an arrow defining the orientation of the molecule. For clarity, most symmetry-related copies of the molecule were removed; those remaining are represented by arrows only. Each arrow is centered on the principal axis of a four-helix bundle and points toward the 80s loop. All three crystal forms show a common, antiparallel packing of the helix bundles. The packing in the trigonal form is exactly antiparallel, while both orthorhombic forms show a slight tilt of the bundle axis relative to the nearest neighbor. The packing pattern propagates as sheets through the crystal. The figure was generated with MOLSCRIPT (Kraulis, 1991), SPOCK (Christopher, 1997), and RASTER3D (Merritt & Bacon, 1997).

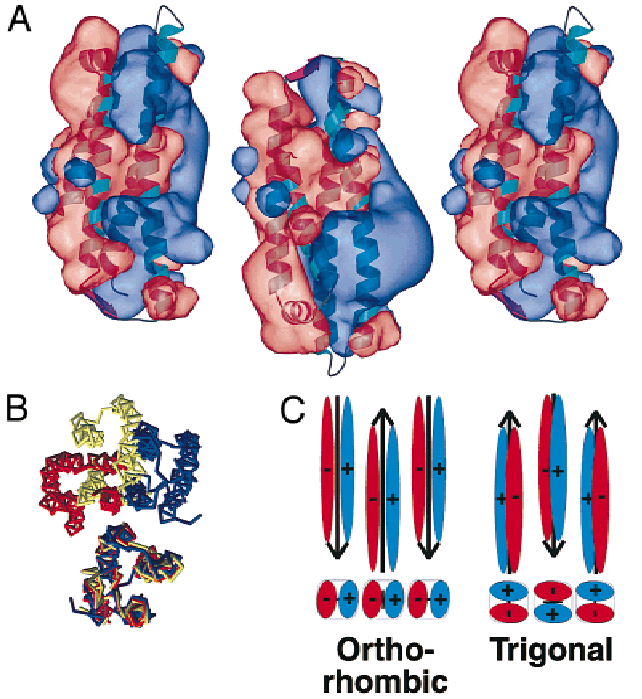

Fig. 5. Electrostatics of packing. **A:** The antiparallel packing arrangement of three symmetry-related four-helix bundles in the ortho-1 crystal form is shown. The bundles are represented as a ribbon diagram and are shown superimposed with semitranslucent isocontours of the electrostatic potential. Red surface represents negative potential (contoured at −3 mV) and blue surface represents positive potential (contoured at 4 mV). For illustrative purposes, the molecules are displayed somewhat apart from their actual packing arrangement. It is apparent that in this arrangement favorable electrostatic interactions take place such that positive and negative electrostatic potentials are juxtaposed. This figure was generated with MOLSCRIPT (Kraulis, 1991), SPOCK (Christopher, 1997), and RASTER3D (Merritt & Bacon, 1997). **B:** Relative orientation of packed molecules in the three crystal forms, superimposed on one molecule of the pseudodimer. Perspective is down the principal axis of the four-helix bundle. The model from the ortho-1 form is shown in red, the trigonal form in magenta, and the ortho-2 form in yellow. While maintaining the commonality of the antiparallel arrangement, packing is not identical in any two crystal forms. The pseudodimers of the ortho-2 and ortho-1 forms differ by a small translational shift, while the pseudodimer of the trigonal crystal form is related to that of ortho-1 by an additional, nearly 90° rotation. This figure was generated with MIDAS (Ferrin et al., 1988). **C:** Schematic of the interactions of the electrostatic lobes in different packing arrangements. The arrow represents the principal axis of the helix bundle, the blue oval represents the positive lobe of electrostatic potential, and the red oval represents the negative lobe of electrostatic potential. The upper sections of the sketch represent the packing plane, the lower sections represent a cross-section thereof (left panel, ortho forms; right panel, trigonal form). In both packing arrangements, positive and negative electrostatic potential are juxtaposed.

These results provide a model for understanding the dynamic behavior of apoE and new insights into how apoE interacts with lipid and how the protein may unfold.

Materials and methods

Purification and expression

The apoE3 1–165 fragment cDNA was prepared from pTV194 (Vogel et al., 1985) by polymerase chain reaction (PCR) mutagenesis and inserted into a T7 bacterial expression system (Studier & Moffatt, 1986). This cDNA actually encodes 166 residues: residues 1–165 of apoE plus the initiating methionine residue at the amino terminus. Non-Se-Met protein was expressed as previously described (Dong et al., 1994). For Se-Met labeling, the pET 165 plasmid was transformed into the methionine auxotroph *Escherichia coli* strain B834(DE). Single colonies were selected and grown in LB medium to log phase. Cell stocks in 20% glycerol were stored at −80 °C. Cells taken from the stock were grown overnight on agar plates containing LB and 100 mg/mL ampicillin. Starter cultures were prepared from several colonies and grown in 5 mL of LB with ampicillin for 1 h. Starter culture (1 mL) was added to 500 mL of methionine-free LeMaster medium (LeMaster & Richards, 1985) supplemented with 250 μL of Kao & Mychayluk vitamin solution (Scapin et al., 1993) and 25 mg of Se-Met. Cultures were grown at 37 °C to optical density (at 600 nm) of 0.6 (12 h), induced with 0.5 mM isopropyl-thio-β-D-galactoside, and harvested after 3 h. Incorporation of Se-Met into the five methionine positions (−1, 64, 68, 108, and 125) was confirmed by electrospray mass spectrometry. The molecular mass increase from 19,402 to 19,639 mass units agrees well with the expected increase resulting from complete Se-Met substitution (calculated, 235; actual 237). The lack of detectable peaks at lower masses indicated that the incorporation was complete at all five sites.

Cell pellets were suspended in 200 volumes of cold sonication buffer [150 mM NaCl, 20 mM Na_2HPO_4, pH 7.4, 25 mM ethylenediaminetetraacetic acid (EDTA), 1% aprotinin (Sigma, St. Louis, Missouri)], 0.1% β-mercaptoethanol (Sigma), and 2 mM phenylmethylsulfonyl fluoride (PMSF) (Sigma) and lysed as previously described (Dong et al., 1994). Lysate fractions were eluted from a Sephacryl S-300 size-exclusion column (300 × 2.5 cm) with 20 mM Tris-Cl buffer (pH 7.4, 4 M guanidine-HCl, 1 mM EDTA, 0.1% β-mercaptoethanol). The apoE 165 fragment was further purified by high-performance liquid chromatography (HPLC) (Gilson, Middleton, Wisconsin) on a 21.5 × 150 mm DEAE column (Supelco, Bellefonte, Pennsylvania), with a linear salt gradient (Dong & Weisgraber, 1996). The purified protein was dialyzed against 20 mM NH_4HCO_3 and concentrated to 5 mg/mL protein stock solution with a Microcon concentrator (Amicon, Beverly, Massachusetts).

Crystallization

The amino-terminal 165 fragment of apoE crystallizes in three forms. After 2–3 days at room temperature, thick rod-shaped crystals are obtained in drops equilibrated against well buffer containing 20–25% polyethylene glycol (PEG)-400 (Fluka, Buchs, Switzerland) and 50 mM Na-cacodylate, pH 5.6. They belong to the orthorhombic space group $P2_12_12_1$ with unit cell dimensions of a = 47.74 Å, b = 55.6 Å, and c = 63.61 Å (ortho-2 form). These crystals can only be obtained from fresh protein stock. Crystals may be obtained from older stock by addition of 1% β-mercaptoethanol to both protein stock and crystallization-well solutions. The resulting crystals have similar morphology to those grown from fresh stock and have the same space group ($P2_12_12_1$) but with cell dimensions of a = 40.8 Å, b = 53.2 Å, and c = 84.8 Å (ortho-1 form). Crystals of a third form (trigonal $P3_121$ with cell dimensions of a and b = 47.54 Å and c = 104.4 Å) have also been obtained. These crystals grow from slightly lower concentrations of PEG-400 (15–20%) than the ortho-1 form and frequently appear in drops where numerous small orthorhombic crystals had formed

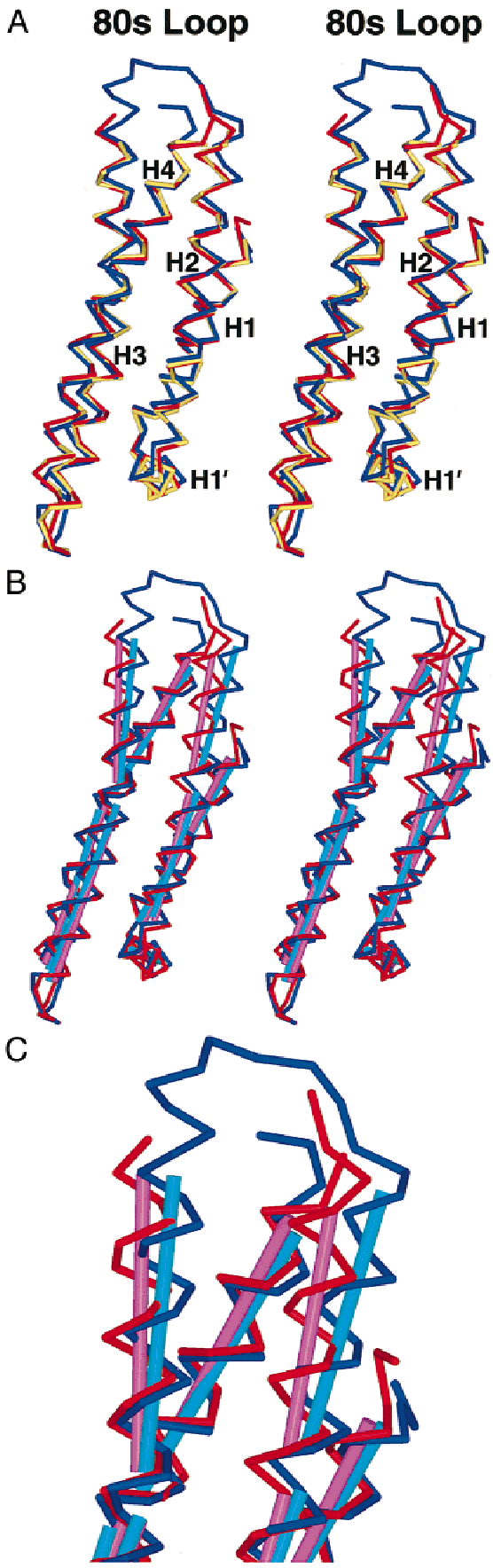

but then disappeared. Crystals of all three forms develop in hanging-drop vapor diffusion experiments (McPherson, 1982) (drops contained 3–5 μL well solution and 3–5 μL protein stock). The Se-Met substituted apoE3 165 fragment was purified by DEAE-HPLC (see Materials and methods), dialyzed against 5 mM NH_4HCO_3, lyophilized, and dissolved in 20 mM NH_4HCO_3. Crystals of ortho-1 and trigonal crystal forms were grown from 5 mg/mL stock in conditions similar to those for native crystals (Table 1).

Data collection, phasing, and refinement

For each of the three crystal forms, native X-ray data were collected with an ADSC multiwire system equipped with two Xuong/Hamlin detectors (Hamlin, 1985), and data were reduced with UCSD data reduction software (Howard et al., 1985). All efforts to arrive at an initial phase set for the trigonal data set by MR [models 1NFN (Dong et al., 1994); 1LPE (Wilson et al., 1991); and ortho-1 form, below] have been unsuccessful [highest correlation with ortho-1 model of 0.19 with R = 60% using EPMR (Kissinger et al., 1999)].

De novo phasing experiments for both the ortho-1 and trigonal crystal forms were performed by using Se-Met MAD (Table 2). Complete, four-wavelength MAD experiments were carried out for the ortho-1 and trigonal crystal forms. Ortho-1 data were collected at Stanford Synchrotron Radiation Laboratory beamline 1–5 from cryo-cooled crystals using a Fuji image plate detector, integrated with DENZO (Otwinowski & Minor, 1997) and scaled with SCALEPACK (Otwinowski & Minor, 1997). MAD data of the ortho-1 form were collected at two remote wavelengths (several hundred electron volts below and above the absorption edge), at the peak of the absorption edge (maximizing f''), and at the maximum of f' as determined by the Kramers–Kronig relation. Ortho-1 crystals diffracted strongly to beyond 2.5 Å, but beamline geometry did not allow for data collection to higher resolution. Data for the trigonal form, to the diffraction limit of 2.0 Å and with good completeness, were collected from cryo-cooled trigonal crystals on Advanced Light Source (ALS) beamline 5.0.2, which is equipped with an Oxford cryostream and a Quantum4 ADSC CCD detector. Reflections were integrated with MOSFLM (CCP4, 1994) and

Fig. 6. Superposition of model structures from three crystal forms. **A:** Stereoview of model structures from each of the three crystal forms, superimposed. Superposition is on all C_α atoms of helical residues in all three models (ortho-1, blue; trigonal, red; ortho-2, yellow). While the ortho-2 and the trigonal models overlap quite well, the ortho-1 model differs significantly. This explains why the trigonal form was a much better MR probe than the ortho-1 form for the determination of the ortho-2 structure. Differences are most significant at the end of the molecule containing the 80s loop. **B:** Stereoview of superposition of the trigonal and ortho-1 models, with the principal axes of the helices shown as rods. The ortho-1 model is blue and the trigonal model is red. The principal axes of the helices are shown in cyan (ortho-1) or magenta (trigonal). The principal axis rods of helices H2, H3, and H4 are split in to two parts, with the split occurring near the amino-terminal end of helix 1. Superposition is on C_αs in section distal to the 80s loop only. This representation emphasizes actual differences in proximity of the 80s loop and demonstrates the similarity of the models in parts distal to the 80s loop. **C:** Close up view of the superposition described in **B**, proximal to the 80s loop. The large deviation between the ends of helices H2 and H3 is apparent. A large deviation is likely to continue into the 80s loop as well but this part of the molecule is not seen in the trigonal structure.

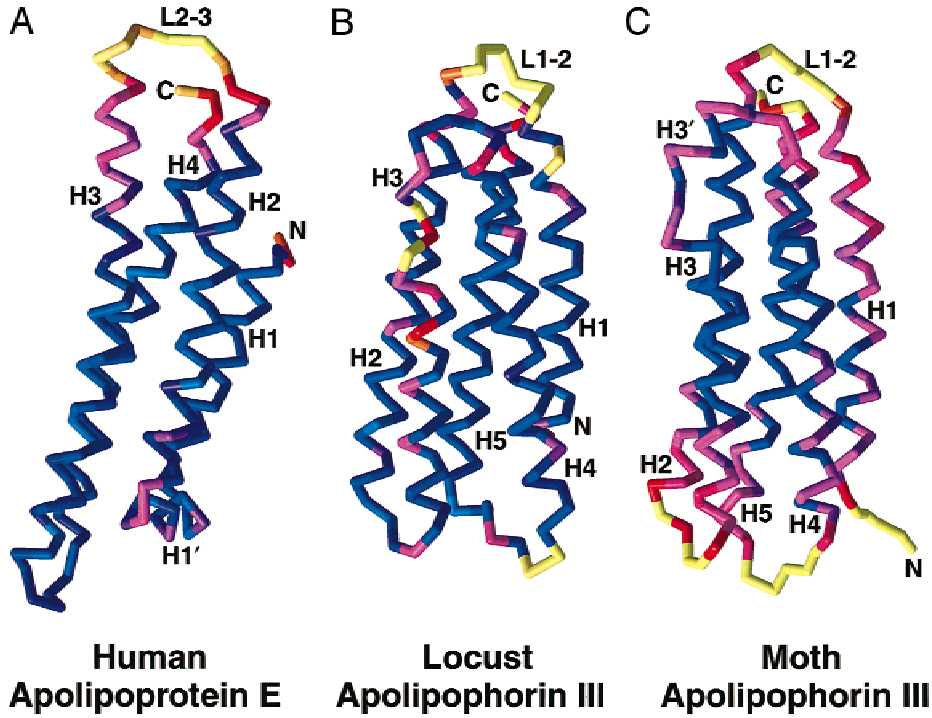

Fig. 7. Apolipoprotein E and apolipophorin III. C_a trace of the (**A**) apoE 165 fragment (ortho-1 form), (**B**) locust apoLpIII (Breiter et al., 1991), and (**C**) moth apoLpIII (Wang et al., 1997). Blue indicates low and yellow high *B* values. *B* values are a measure of the mean displacement of an atom, and high values indicate areas of high mobility. (**C**) For the NMR struture, the isotropic *B*-factor equivalents have been calculated from the mean-square coordinate differences between the models ($B_{iso} = 8\pi^2(\langle r_x^2\rangle + \langle r_y^2\rangle + \langle r_z^2\rangle)/3$). The NMR model coordinates have been kindly provided by J. Wang, B.D. Sykes and R.O. Ryan (unpubl. data). In the case of apoE, additional support for the flexibility of the 80s loop (L2-3, **A**) originates from the different conformations this part of the molecule assumes in different crystal forms (Fig. 6B). The figure clearly shows the similarity of the flexibility in the regions presumed to initiate the opening of the helix bundle both molecules (top of the models). The connection between distinct helices H3 and H3′ in moth apoLpIII (**C**) corresponds to a region of high mobility in locust apoLpIII helix H3 (**B**). This figure was generated with MIDAS (Ferrin et al., 1988).

scaled with SCALA (Kabsch, 1988) (wavelengths were selected as described above).

Se positions were initially determined and phase calculation was performed with SOLVE (Terwilliger & Berendzen, 1999) on the four-wavelength MAD data sets. Native data (Table 1) were included in the phasing experiment, and phases were recalculated with SHARP (de La Fortelle & Bricogne, 1997). Phase calculations gave the best overall figure of merit if atom positions determined by SOLVE were fixed during SHARP refinement. Judging from phasing power and figure of merit, the phase quality for both ortho-1 and trigonal crystal forms is exceptional to ~2.5 Å. Atomic models for the ortho-1 and trigonal structures were manually traced with XtalView (McRee, 1992) into solvent-flattened maps generated by DM (Cowtan & Main, 1996). Density modification was repeated with SOLOMON solvent flipping (Abrahams & Leslie, 1996), yielding far superior maps (Fig. 2A). Models were iteratively built into maps generated by a slightly modified wARP procedure (Perrakis et al., 1997) (Fig. 2B). Initial phase estimates were determined for the ortho-2 data set by MR with EPMR using the trigonal model (correlation coefficient 0.67, *R*-value 42%). Since wARP is not applicable given the data/parameter ratio at the resolution of the ortho-2 data, this model was iteratively built into maximum-likelihood (CCP4, 1994; Murshudov et al., 1997) FWT/PHWT, DELFWT/DELPHWT, or shake-omit maps (Zeng et al., 1997). Shake-omit maps were generated by perturbing atomic coordinates by ±0.5 Å (typical RMSD after shaking was ~0.25 Å) to reduce the phase bias before the Fourier transform, removing 10% of the model, then applying rigid body refinement in REFMAC (Murshudov et al., 1997) to generate the maximum-likelihood structure factors. After several cycles of rebuilding, water molecules were added either by ARP (Lamzin & Wilson, 1993) or by manual placement in XtalView (McRee, 1992). Each model structure was refined with REFMAC (CCP4, 1994) and/or X-PLOR 3.851. Final coordinates are from X-PLOR refinement with solvent correction and overall anisotropic B correction applied. Despite the use of a maximum-likelihood target function in REFMAC (absent in X-PLOR 3.851), the best final *R* and R_{free} were obtained by initial refinement with REFMAC, followed by X-PLOR solvent correction, overall anisotropic B correction, and final individual B refinement. Careful pruning of water molecules based on real space fit correlation significantly affected the R/R_{free} ratio.

Acknowledgments

We thank Michelle Corzett [Lawrence Livermore National Laboratory (LLNL)] for assistance with the seleno-methionine protein expression; Carl Cork, Gerry McDermott, and Thomas E. Earnest for beam line support at the Advanced Light Source; Tom Terwilliger [Los Alamos National Laboratory (LANL)] for advice on his new automated phasing program SOLVE; John Carroll and Stephen Gonzales for graphic arts; Gary Howard and Stephen Ordway for editorial assistance; and Brian Auerbach for manu-

script preparation. This work was supported under the auspices of the U.S. Department of Energy (DOE) at LLNL under contract no. W-7405-ENG-48 and Grant NS35939 from the National Institutes of Health (NIH). Work at the Stanford Synchrotron Radiation Laboratory (SSRL) was funded by the DOE, Office of Basic Energy Sciences. The SSRL Biotechnology Program is supported by the NIH, Biomedical Research Technology Program, Division of Research Resources. Further support is provided to SSRL by DOE, Office of Biological and Environmental Research. The Macromolecular Crystallography Facility at the Advanced Light Source is principally funded by the Office of Biological and Environmental Research of DOE with contributions from Lawrence Berkeley National Laboratory, Amgen, Roche Biosciences, University of California at Berkeley, Genetics Institute, and LLNL. Mass spectra were provided by the UCSF Mass Spectrometry Facility (A.L. Burlingame, Director) supported by the Biomedical Research Technology Program of the National Center for Research Resources, NIH NCRR BRTP RR01614. Special thanks are due to J. Wang, B.D. Sykes, and R.O. Ryan for providing their unpublished NMR coordinates of apoLpIII.

References

Abrahams JP, Leslie AGW. 1996. Methods used in the structure determination of bovine mitochondrial F_1 ATPase. *Acta Crystallogr D 52*:30–42.

Aggerbeck LP, Wetterau JR, Weisgraber KH, Wu C-SC, Lindgren FT. 1988. Human apolipoprotein E3 in aqueous solution. II. Properties of the amino- and carboxyl-terminal domains. *J Biol Chem 263*:6249–6258.

Avila EM, Holdsworth G, Sasaki N, Jackson RL, Harmony JAK. 1982. Apoprotein E suppresses phytohemagglutinin-activated phospholipid turnover in peripheral blood mononuclear cells. *J Biol Chem 257*:5900–5909.

Blundell TL, Johnson LN. 1976. *Protein crystallography*. San Diego: Academic Press. p 565.

Breiter DR, Kanost MR, Benning MM, Wesenberg G, Law JH, Wells MA, Rayment I, Holden HM. 1991. Molecular structure of an apolipoprotein determined at 2.5-Å resolution. *Biochemistry 30*:603–608.

Brünger AT. 1992a. Free *R* value: A novel statistical quantity for assessing the accuracy of crystal structures. *Nature 355*:472–475.

Brünger AT. 1992b. *X-PLOR, Version 3.1. A system for X-ray crystallography and NMR*. New Haven, CT: Yale University Press.

CCP4 (Collaborative Computational Project Number 4). 1994. The CCP4 suite: Programs for protein crystallography. *Acta Crystallogr D 50*:760–763.

Christopher JA. 1997. *The SPOCK program manual. SPOCK: The structural properties observation and calculation kit*.

Corder EH, Saunders AM, Strittmatter WJ, Schmechel DE, Gaskel PC, Small GW, Roses AD, Haines JL, Pericak-Vance MA. 1993. Gene dose of apolipoprotein E type 4 allele and the risk of Alzheimer's disease in late onset families. *Science 261*:921–923.

Cowtan KD, Main P. 1996. Phase combination and cross validation in iterated density-modification calculations. *Acta Crystallogr D 52*:43–48.

de La Fortelle E, Bricogne G. 1997. Maximum-likelihood heavy-atom parameter refinement for multiple isomorphous replacement and multiwavelength anomalous diffraction methods. *Methods Enzymol 276*:472–494.

De Pauw M, Vanloo B, Weisgraber KH, Rosseneu M. 1995. Comparison of lipid-binding and lecithin:cholesterol acyltransferase activation of the amino- and carboxyl-terminal domains of human apolipoprotein E3. *Biochemistry 34*:10953–10960.

Dong L-M, Parkin S, Trakhanov SD, Rupp B, Simmons T, Arnold KS, Newhouse YM, Innerarity TL, Weisgraber KH. 1996. Novel mechanism for defective receptor binding of apolipoprotein E2 in type III hyperlipoproteinemia. *Nat Struct Biol 3*:718–722.

Dong L-M, Weisgraber KH. 1996. Human apolipoprotein E4 domain interaction. Arginine 61 and glutamic acid 255 interact to direct the preference for very low density lipoproteins. *J Biol Chem 271*:19053–19057.

Dong L-M, Wilson C, Wardell MR, Simmons T, Mahley RW, Weisgraber KH, Agard DA. 1994. Human apolipoprotein E. Role of arginine 61 in mediating the lipoprotein preferences of the E3 and E4 isoforms. *J Biol Chem 269*:22358–22365.

Eichner JE, Kuller LH, Orchard TJ, Grandits GA, McCallum LM, Ferrel RE, Neaton JD. 1993. Relation of apolipoprotein E phenotype to myocardial infarction and mortality from coronary artery disease. *Am J Cardiol 71*: 160–165.

Ferrin TE, Huang CC, Jarvis LE, Langridge R. 1988. The MIDAS display system. *J Mol Graph* 6:13–27.

Forstner M, Peters-Libeu C, Contreras-Forrest E, Newhouse YM, Knapp M, Rupp B, Weisgraber KH. 1999. Carboxyl-terminal domain of human apolipoprotein E: Expression, purification, and crystallization. *Protein Expr Purif 17*:267–272.

Hamlin R. 1985. Multiwire area X-ray diffractometers. *Methods Enzymol 114*:416–452.

Harris NL, Presnell SR, Cohen FE. 1994. Four helix bundle diversity in globular proteins. *J Mol Biol 236*:1356–1368.

Hendrickson WA, Ogata CM. 1997. Phase determination from multiwavelength anomalous diffraction measurements. *Methods Enzymol 276*:494–516.

Howard AJ, Nielsen C, Xuong NH. 1985. Software for a diffractometer with multiwire area detector. *Methods Enzymol 114*:452–472.

Hui DY, Harmony JAK, Innerarity TL, Mahley RW. 1980. Immunoregulatory plasma lipoproteins. Role of apoprotein E and apoprotein B. *J Biol Chem 255*:11775–11781.

Innerarity TL, Friedlander EJ, Rall SC Jr, Weisgraber KH, Mahley RW. 1983. The receptor-binding domain of human apolipoprotein E. Binding of apolipoprotein E fragments. *J Biol Chem 258*:12341–12347.

Innerarity TL, Pitas RE, Mahley RW. 1979. Binding of arginine-rich E apoprotein after recombination with phospholipid vesicles to the low density lipoprotein receptors of fibroblasts. *J Biol Chem 254*:4186–4190.

Ishigami M, Swertfeger DK, Granholm NA, Hui DY. 1998. Apolipoprotein E inhibits platelet-derived growth factor-induced vascular smooth muscle cell migration and proliferation by suppressing signal transduction and preventing cell entry to G_1 phase. *J Biol Chem 273*:20156–20161.

Kabsch W. 1988. Evaluation of single-crystal X-ray diffraction data from a position-sensitive detector. *J Appl Crystallogr 21*:916–924.

Kissinger CR, Gehlhaar DK, Fogel DB. 1999. Rapid automated molecular replacement by evolutionary search. *Acta Crystallogr D 55*:484–491.

Kraulis PJ. 1991. MOLSCRIPT: A program to produce both detailed and schematic plots of protein structures. *J Appl Crystallogr 24*:946–950.

Lamzin VS, Wilson KS. 1993. Automated refinement of protein models. *Acta Crystallogr D 49*:129–147.

LeMaster DM, Richards FM. 1985. ^1H–^{15}N heteronuclear NMR studies of *Escherichia coli* thioredoxin in samples isotopically labeled by residue type. *Biochemistry 24*:7263–7268.

Luc G, Bard J-M, Arveiler D, Evans A, Cambou J-P, Bingham A, Amouyel P, Schaffer P, Ruidavets J-B, Cambien F, Fruchart J-C, Ducimetiere P. 1994. Impact of apolipoprotein E polymorphism on lipoproteins and risk of myocardial infarction. The ECTIM study. *Arterioscler Thromb 14*:1412–1419.

Luzzati V. 1953. Resolution d'une structure cristalline lorsque les positions d'une partie des atomes sont connues: Traitement statistique. *Acta Crystallogr 6*:142–152.

Mahley RW. 1988. Apolipoprotein E: Cholesterol transport protein with expanding role in cell biology. *Science 240*:622–630.

Mahley RW, Rall SC Jr. 1995. Type III hyperlipoproteinemia (dysbetalipoproteinemia): The role of apolipoprotein E in normal and abnormal lipoprotein metabolism. In: Scriver CR, Beaudet AL, Sly WS, Valle D, eds. *The metabolic and molecular bases of inherited disease*, 7th ed. New York: McGraw-Hill. pp 1953–1980.

Mayeux R, Ottman R, Maestre G, Ngai C, Tang M-X, Ginsberg H, Chun M, Tycko B, Shelanski M. 1995. Synergistic effects of traumatic head injury and apolipoprotein-e4 in patients with Alzheimer's disease. *Neurology 45*:555–557.

McPherson A. 1982. *Preparation and analysis of protein crystals*, New York: John Wiley & Sons.

McRee DE. 1992. A visual protein crystallographic software system for X11/Xview. *J Mol Graph 10*:44–46.

Merritt EA, Bacon DJ. 1997. Raster3D: Photorealistic molecular graphics. *Methods Enzymol 277*:505–524.

Murshudov GN, Vagin AA, Dodson EJ. 1997. Refinement of macromolecular structures by the maximum-likelihood method. *Acta Crystallogr D 53*:240–255.

Narayanaswami V, Wang J, Kay CM, Scraba DG, Ryan RO. 1996. Disulfide bond engineering to monitor conformational opening of apolipophorin III during lipid binding. *J Biol Chem 271*:26855–26862.

Narayanaswami V, Wang J, Schieve D, Kay CM, Ryan RO. 1999 A molecular trigger of lipid binding-induced opening of a helix bundle exchangeable apolipoprotein. *Proc Natl Acad Sci USA 96*:4366–4371.

Otwinowski Z, Minor W. 1997. Processing of X-ray diffraction data collected in oscillation mode. *Methods Enzymol 276*:307–326.

Parkin S, Hope H. 1998. Macromolecular cryocrystallography: Cooling, mounting, storage and transportation of crystals. *J Appl Crystallogr 31*:945–953.

Perrakis A, Sixma TK, Wilson KS, Lamzin VS. 1997. *wARP*: Improvement and extension of crystallographic phases by weighted averaging of multiple-refined dummy atomic models. *Acta Crystallogr D 53*:448–455.

Raffaï R, Maurice R, Weisgraber, KH, Innerarity T, Wang X, MacKenzie R, Hirama T, Watson D, Rassart E, Milne R. 1995. Molecular characterization of two monoclonal antibodies specific for the LDL receptor-binding site of human apolipoprotein E. *J Lipid Res 36*:1905–1918.

Rall SC Jr, Mahley RW. 1992. The role of apolipoprotein E genetic variants in lipoprotein disorders. *J Intern Med 231*:653–659.

Rall SC Jr, Weisgraber KH, Mahley RW. 1982. Human apolipoprotein E. The complete amino acid sequence. *J Biol Chem 257*:4171–4178.

Ramachandran GN, Ramakrishnan C, Sasisekharan V. 1963. Stereochemistry of polypeptide chain configurations. *J Mol Biol 7*:95–99.

Raussens V, Fisher CA, Goormaghtigh E, Ryan RO, Ruysschaert J-M. 1998. The low density lipoprotein receptor active conformation of apolipoprotein E. Helix organization in N-terminal domain-phospholipid disc particles. *J Biol Chem 273*:25825–25830.

Reyland ME, Williams DL. 1991. Suppression of cAMP-mediated signal transduction in mouse adrenocortical cells which express apolipoprotein E. *J Biol Chem 266*:21099–21104.

Saunders AM, Strittmatter WJ, Schmechel D, St George-Hyslop PH, Pericak-Vance MA, Joo SH, Rosi BL, Gusella JF, Crapper-MacLachlan DR, Alberts MJ, et al. 1993. Association of apolipoprotein E allele e4 with late-onset familial and sporadic Alzheimer's disease. *Neurology 43*:1467–1472.

Scapin G, Sacchettini JC, Dessen A, Bhatia M, Grubmeyer C. 1993. Primary structure and crystallization of orotate phosphoribosyltransferase from *Salmonella typhimurium*. *J Mol Biol 230*:1304–1308.

Segrest JP, Garber DW, Brouillette CG, Harvey SC, Anantharamaiah GM. 1994. The amphipathic a helix: A multifunctional structural motif in plasma apolipoproteins. *Adv Protein Chem 45*:303–369.

Segrest JP, Jones MK, De Loof H, Brouillette CG, Venkatachalapathi YV, Anantharamaiah GM. 1992. The amphipathic helix in the exchangeable apolipoproteins: A review of secondary structure and function. *J Lipid Res 33*:141–166.

Slooter AJC, Tang M-X, van Duijn CM, Stern Y, Ott A, Bell K, Bretele MMB, Van Broeckhoven C, Tatemichi TK, Tycko B, et al. 1997. Apolipoprotein E4 and the risk of dementia with stroke. A population-based investigation. *J Am Med Assoc 277*:818–821.

Strittmatter WJ, Saunders AM, Schmechel D, Pericak-Vance M, Enghild J, Salvesen GS, Roses AD. 1993. Apolipoprotein E: High-avidity binding to *b*-amyloid and increased frequency of type 4 allele in late-onset familial Alzheimer disease. *Proc Natl Acad Sci USA 90*:1977–1981.

Studier FW, Moffatt BA. 1986. Use of bacteriophage T7 RNA polymerase to direct selective high-level expression of cloned genes. *J Mol Biol 189*:113–130.

Teasdale GM, Nicoll JAR, Murray G, Fiddes M. 1997. Association of apolipoprotein E polymorphism with outcome after head injury. *Lancet 350*:1069–1071.

Terwilliger TC, Berendzen J. 1999. Automated MAD and MIR structure solution. *Acta Crystallogr D 55*:849–861.

Trakhanov S, Parkin S, Raffaï R, Milne R, Newhouse YM, Weisgraber KH, Rupp B. 1999. Structure of a monoclonal 2E8 Fab antibody fragment specific for the low-density lipoprotein-receptor binding region of apolipoprotein E refined at 1.9 Å. *Acta Crystallogr D 55*:122–128.

Utermann G, Hardewig A, Zimmer F. 1984. Apolipoprotein E phenotypes in patients with myocardial infarction. *Hum Genet 65*:237–241.

Vogel T, Weisgraber KH, Zeevi MI, Ben-Artzi H, Levanon AZ, Ral SC Jr, Innerarity TL, Hui DY, Taylor JM, Kanner D, et al. 1985. Human apolipoprotein E expression in *Escherichia coli*: Structural and functional identity of the bacterially produced protein with plasma apolipoprotein E. *Proc Natl Acad Sci USA 82*:8696–8700.

Vriend G. 1990. WHAT IF: A molecular modeling and drug design program. *J Mol Graphics 8*:52–56.

Wang J, Gagné SM, Sykes BD, Ryan RO. 1997. Insight into lipid surface recognition and reversible conformational adaptations of an exchangeable apolipoprotein by multidimensional heteronuclear NMR techniques. *J Biol Chem 272*:17912–17920.

Weisgraber KH. 1990. Apolipoprotein E distribution among human plasma lipoproteins: Role of the cysteine-arginine interchange at residue 112. *J Lipid Res 31*:1503–1511.

Weisgraber KH. 1994. Apolipoprotein E: Structure–function relationships. *Adv Protein Chem 45*:249–302.

Weisgraber KH, Lund-Katz S, Phillips MC. 1992. Apolipoprotein E: Structure-function correlations. In: Miller NE, Tall AR, eds. *High density lipoproteins and atherosclerosis III*. Amsterdam: Elsevier Science Publishers. pp 175–181.

Weisgraber KH, Rall SC Jr, Mahley RW. 1981. Human E apoprotein heterogeneity. Cysteine-arginine interchanges in the amino acid sequence of the apo-E isoforms. *J Biol Chem 256*:9077–9083.

Wetterau JR, Aggerbeck LP, Rall SC Jr, Weisgraber KH. 1988. Human apolipoprotein E3 in aqueous solution. I. Evidence for two structural domains. *J Biol Chem 263*:6240–6248.

Wilson C, Mau T, Weisgraber KH, Wardell MR, Mahley RW, Agard DA. 1994. Salt bridge relay triggers defective LDL receptor binding by a mutant apolipoprotein. *Structure 2*:713–718.

Wilson C, Wardell MR, Weisgraber KH, Mahley RW, Agard DA. 1991. Three-dimensional structure of the LDL receptor-binding domain of human apolipoprotein E. *Science 252*:1817–1822.

Zeng Z-H, Castaño AR, Segelke BW, Stura EA, Peterson PA, Wilson IA. 1997. Crystal structure of mouse CD1: An MHC-like fold with a large hydrophobic binding groove. *Science 277*:339–345.